Structure of Orthoreovirus RNA Chaperone σNS, a Component of Viral Replication Factories

Boyang Zhao,[1] Liya Hu,[2] Soni Kaundal,[2] Neetu Neetu, Christopher H. Lee,[3,4] Xayathed Somoulay,[3,4] Banumathi Sankaran[6], Gwen M. Taylor,[4,5] Terence S. Dermody,[3,4,5*] and B. V. Venkataram Prasad[1,2*]

[1]Department of Molecular Virology and Microbiology, Baylor College of Medicine

[2]Verna and Marrs Mclean Department of Biochemistry and Molecular Pharmacology, Baylor College of Medicine

[3]Department of Microbiology and Molecular Genetics, University of Pittsburgh School of Medicine

[4]Institute of Infection, Inflammation, and Immunity, UPMC Children's Hospital of Pittsburgh

[5]Department of Pediatrics, University of Pittsburgh School of Medicine

[6]Berkeley Center for Structural Biology, Molecular Biophysics and Integrated Bioimaging, Lawrence Berkeley Laboratory, Berkeley, CA, U.S.A.

*Corresponding authors (terence.dermody@chp.edu; vprasad@bcm.edu)

Abstract

The reovirus σNS RNA-binding protein is required for formation of intracellular compartments during viral infection that support viral genome replication and capsid assembly. Despite its functional importance, a mechanistic understanding of σNS is lacking. We conducted structural and biochemical analyses of an R6A mutant of σNS that forms dimers instead of the higher-order oligomers formed by wildtype (WT) σNS. The crystal structure of selenomethionine-substituted σNS-R6A reveals that the mutant protein forms a stable antiparallel dimer, with each subunit having a well-folded central core and a projecting N-terminal arm. The dimers interact with each other by inserting the N-terminal arms into a hydrophobic pocket of the neighboring dimers on either side to form a helical assembly that resembles filaments of WT σNS in complex with RNA observed using cryo-EM. The interior of the crystallographic helical assembly is positively charged and of appropriate diameter to bind RNA. The helical assembly is disrupted by bile acids, which bind to the same hydrophobic pocket as the N-terminal arm, as demonstrated in the crystal structure of σNS-R6A in complex with bile acid. This finding suggests that the N-terminal arm functions in conferring context-dependent oligomeric states of σNS, which is supported by the structure of σNS lacking the N-terminal arm. We discovered that σNS displays RNA helix destabilizing and annealing activities, likely essential for presenting mRNA to the viral RNA-dependent RNA polymerase for genome replication. The RNA chaperone activity is reduced by bile acids and abolished by N-terminal arm deletion, suggesting that the activity requires formation of σNS oligomers. Our studies provide structural and mechanistic insights into the function of σNS in reovirus replication.

43 ## Introduction

44 Most viruses that replicate in the cytoplasm of host cells form neoorganelles that serve as sites of
45 viral genome replication and particle assembly. These highly specialized viral factory (VF)
46 structures concentrate viral replication proteins and nucleic acids, limit activation of cell-intrinsic
47 defenses, and coordinate release of progeny particles. Both viral and cellular proteins contribute
48 to VF formation and orchestrate viral replication functions.

49 Mammalian orthoreoviruses (reoviruses) are members of the Orthoreovirus genus in the
50 *Reoviridae* family. Reoviruses are classified into four serotypes based on sequence and
51 antigenicity of the σ1 viral attachment protein and include prototype strains type 1 Lang, type 2
52 Jones, type 3 Dearing, and type 4 Ndelle [1]. While reovirus can infect many mammalian species,
53 including humans, symptomatic infection develops only in neonatal mammals and human infants
54 and children [2]. Infection by some reovirus strains appears to induce the development of celiac
55 disease, a complex immune disorder characterized by an immune response to dietary gluten that
56 can damage the intestinal lining and result in diarrhea and malabsorption [3]. Reovirus can induce
57 apoptosis, necroptosis, and pyroptosis in tumor cells by activating programmed cell death
58 pathways [4]. Because of these characteristics, reovirus was one of the first viruses used as an
59 oncolytic agent [5].

60 Reovirus forms nonenveloped particles with an icosahedral capsid, 800 Å in diameter,
61 consisting of two concentric protein layers and distinctive turret-like spikes projecting from the
62 twelve icosahedral vertices. Encapsidated within the innermost protein layer is the viral genome,
63 consisting of ten segments of linear double-stranded (ds) RNA, which encode eleven viral
64 proteins. Eight of these proteins are structural and form the two capsid layers, turret, attachment
65 protein, and an internally located RNA-dependent RNA polymerase. There are three

66 nonstructural proteins that function to promote viral replication. Reovirus replication occurs in
67 the cytoplasm. After binding to cellular receptors, the virus particle enters many types of cells by
68 clathrin-mediated endocytosis [6]. Within endosomes, proteolysis of outer-capsid proteins yields
69 infectious subvirion particles, which penetrate endosomal membranes to release transcriptionally
70 active viral cores into the cytoplasm [7]. Following transcription of dsRNA segments within the
71 core interior, capped viral mRNAs are extruded through the turrets into the cytoplasm. The
72 capped transcripts serve as templates for translation as well as synthesis of minus-strand genomic
73 RNA by the viral polymerase to produce the dsRNA genome segments. Assortment of the
74 genome segments into progeny core particles and addition of outer-capsid proteins occur inside
75 VFs. Nonstructural proteins σNS and μNS are required to nucleate these compartments during
76 infection.

77 In addition to its essential function in formation of viral replication factories, σNS
78 recruits viral RNA [8] and both the eukaryotic translation initiation factor 3 subunit A (eIF3A) and
79 the ribosomal subunit pS6R to enhance viral RNA translation [9]. Its association with the major
80 stress granule effector protein, Ras-GAP SH3-binding protein 1 (G3BP1), disrupts stress granule
81 formation, which relieves a block to reovirus replication [10]. σNS binds viral ssRNA
82 nonspecifically [11], protects ssRNAs from degradation, and ferries viral mRNAs to VFs [12]. A
83 mechanistic understanding of this multifunctional protein is lacking without its atomic-resolution
84 structure. Our previous studies using cryo-EM show that σNS forms heterogeneous, higher-order
85 oligomers and, when associated with ssRNA, it forms filamentous structures [12]. However, neither
86 the unliganded nor the RNA-bound form of σNS are conducive to high-resolution structural
87 studies.

88 We found that an arginine-to-alanine mutation at residue 6 in σNS (σNS-R6A) prevents
89 RNA binding and formation of higher-order oligomers, thus facilitating σNS structural and
90 biochemical characterization. From these analyses, we discovered that domain-swapping
91 interactions of the flexible N-terminal arms of σNS dimers facilitate the association of dimers
92 into filamentous structures that can bind ssRNA. Moreover, we found that such assemblies are
93 required for an RNA chaperone activity of σNS, which we postulate is required for reovirus
94 replication. Bile acids bind to the same hydrophobic pocket as the N-terminal arms and disrupt
95 filament formation and impede RNA chaperone activity. Collectively, these findings provide
96 mechanistic understanding of σNS function in reovirus replication and provide clues about
97 dsRNA synthesis in a *Reoviridae* virus.
98

99 ## Results

100 **R6A mutation disrupts σNS RNA binding and oligomerization**

101 Initial attempts to crystalize wildtype (WT) σNS were unsuccessful due to binding of the protein
102 to RNA, which leads to formation of higher-order oligomers that disassemble into heterogeneous
103 populations during purification and crystallization. The N-terminal 38 residues of σNS include
104 several amino acids required for σNS binding to RNA [12]. These residues are conserved in all
105 reovirus σNS sequences reported to date [13]. We previously engineered σNS mutants incapable of
106 binding RNA to assess the requirement of σNS RNA-binding activity in reovirus replication [8].
107 The σNS-R6A mutant does not distribute to VFs and fails to transport viral mRNA to these
108 structures [8]. Based on its lack of RNA-binding capacity, we selected the σNS-R6A mutant for
109 purification and crystallization. Expression and purification of σNS-R6A yielded pure and
110 homogenous recombinant protein. Following anion-exchange chromatography, we compared

111 recombinant WT σNS and σNS-R6A for interactions with nucleic acid (**Fig. 1a**). Anion-
112 exchange chromatography of WT σNS showed two peaks in contrast to that of the σNS-R6A
113 mutant, which showed one peak, consistent with the failure of σNS-R6A to bind RNA. Size-
114 exclusion chromatography of WT σNS following anion-exchange chromatography, yielded an
115 oligomer of a size corresponding to a decamer (**Fig. 1b**) in contrast to σNS-R6A, which showed
116 a peak corresponding to a dimer (~80 kDa). Surprisingly, the selenomethionine (Se-Met)-
117 substituted σNS-R6A, which we purified for crystallization attempts, showed a size-exclusion
118 chromatography profile suggesting multimeric association with a peak corresponding to an
119 octamer.
120

121 **σNS forms a stable core structure with a flexible N-terminal arm**

122 To gain a mechanistic understanding of biological functions of σNS, we determined the structure
123 of the σNS-R6A mutant. Although we successfully obtained diffracting crystals of σNS-R6A,
124 determination of the structure by molecular replacement was not possible without suitable
125 phasing models. Accordingly, we proceeded with Se-Met-substituted σNS-R6A and determined
126 the structure using SAD phasing methods to a resolution of 3.0 Å (**Table 1**). Se-Met σNS-R6A
127 crystallized in the space group $P6_5$ with two molecules in the asymmetric unit. The crystal
128 structure of σNS-R6A reveals a stable core structure with a protruding N-terminal arm (**Fig. 2a**).
129 The core structure is formed by 13 β-strands and 19 α-helices connected by β- or γ-turns (**Fig.
130 2b**). The β-strands form four, antiparallel β-sheets on the surface of a globular central body
131 formed by α-helices. The N-terminal residues 4 to 11 form the first helix, which is connected to a
132 short strand by a seven-residue loop. A nine-residue β-hairpin follows the short strand and
133 connects to the first antiparallel sheet of σNS. This antiparallel sheet from residues 30 to 40

134 together with the N-terminus forms a cleft of about ~ 25 Å in width. There are several long
135 helices connected by β-turns from residues 245 to 335. The C-terminal region of σNS is
136 connected to helix 19 by a γ-turn and consists of four strands.

137 To define flexible regions of σNS, we conducted molecular dynamics simulations based
138 on the σNS-R6A structure. The simulations showed that the σNS N-terminus displays five-fold
139 greater flexibility relative to the other regions of the protein, as assessed by the root mean square
140 flexibility (RMSF) (**Fig. 2c**). The β-sheet connected to the N-terminal loop represents a second
141 region of flexibility, suggesting that σNS contains a flexible N-terminal region. Interestingly, the
142 addition of ssRNA into the simulation diminishes the RMSF of the N-terminus by about 25%.
143

144 **σNS forms a stable dimer**

145 The crystallographic asymmetric unit contains two σNS-R6A subunits that form an antiparallel
146 dimer related by non-crystallographic two-fold symmetry, with the N-terminal arms projecting
147 away at either end (**Fig. 3a**). The σNS-R6A dimer is stabilized by an interface with a calculated
148 buried surface area (BSA) of 1853 $Å^2$, indicating a biologically relevant oligomer that is stable in
149 solution. The σNS-R6A dimer is stabilized mainly by hydrogen bonds between multiple residues
150 (**Fig. 3b**). Since the dimer interface displays two-fold symmetry, equivalent clusters of residues
151 are formed on both sides of the interface. These clusters include hydrophobic residues (Gly 148
152 and Val 160) and polar residues (Arg 67, Arg 159, His 164, Asp 168, and Glu 243) (**Fig. 3c**),
153 typical of intersubunit interactions in stable homodimeric proteins [14]. These observations suggest
154 that σNS dimers with protruding N-terminal arms are the building blocks of higher-order
155 structures.
156

157 **σNS dimers form a helical assembly by domain-swapping N-terminal arm interactions**

158 The packing of the Se-Met σNS-R6A dimeric subunits in the crystals shows a helical
159 organization with a ~ 40 Å central cavity formed by domain-swapping interactions between the
160 N-terminal arms of the neighboring dimers (**Fig. 4a-d**). The overall diameter of the helical
161 assembly is ~ 150 Å. Interactions of σNS to form helical assemblies are consistent with previous
162 observations using cryo-EM, indicating that σNS forms filamentous structures in the presence of
163 RNA [12]. Such helical assemblies were not expected for the σNS-R6A mutant, as it does not bind
164 RNA and forms only dimers in solution. However, the size-exclusion chromatography profile of
165 Se-Met-substituted σNS-R6A clearly showed that it forms higher-order oligomers in solution as
166 observed with WT σNS (**Fig. 1b**). It is possible that increased hydrophobicity due to substitution
167 of a selenium atom for a sulfur atom[15] in Met 1 coupled with crystal-packing forces restrict the
168 flexibility of the N-terminal arms and allow this region of the protein to stabilize a multimeric
169 association.

170

171 **Bile acid derivatives disrupt σNS filament formation**

172 We observed that the native σNS-R6A crystals, without Se-Met substitution, crystallized in the
173 $P4_1$ space group instead of $P6_5$. Interestingly, native σNS-R6A crystallized only in conditions
174 with bile acid derivatives in contrast to Se-Met σNS-R6A, which crystallized without these
175 additives. Structure determination of native σNS-R6A, using the Se-Met σNS-R6A structure as a
176 molecular replacement model, showed that native σNS-R6A also forms an antiparallel dimer,
177 with two bile acid moieties bound to each subunit in a groove located near the σNS C-terminus
178 (**Fig. 5a**, sites 1 and 2). Binding of bile acid molecules is mediated by hydrophobic contacts with
179 residues Thr 107, Glu 110, Leu 111, Ser 114, Gly 203, Leu 204, Tyr 240, Glu 242, Ala 245, and

180 Glu 246 (**Fig. 5b**). Remarkably, in contrast to the Se-Met σNS-R6A structure, the N-terminal
181 arm is disordered and not observed in the native σNS-R6A structure. Instead of the distinct
182 helical assembly in the structure of Se-Met σNS-R6A, native σNS-R6A dimers crystallized with
183 bile acid show sheet-like packing (**Fig. 5c).** Further examination of the structure showed that one
184 of the bile acid molecules strikingly occupies the same location in the core domain as the N-
185 terminal arm required to form helical assemblies, suggesting that bile acid competes with the N-
186 terminal arm to disrupt the helical assembly formation observed in the Se-Met σNS-R6A
187 structure (**Fig. 5d-f**).
188

189 **The σNS N-terminal arm is required for multimeric association**

190 To provide additional evidence for the role of domain-swapping interactions of the N-terminal
191 arms in forming oligomeric assemblies, we engineered a deletion construct, σNS-ΔN17, by
192 truncating the N-terminal 17 residues of the protein. The σNS-ΔN17 mutant formed dimers in
193 solution and, interestingly, it also crystallized in the presence of bile acid derivatives. The σNS-
194 ΔN17 crystal structure determined using molecular replacement showed a dimer formed by a
195 central core identical to that in the structures of Se-Met or native σNS-R6A (**Fig. 5g**) with two
196 bound bile acid moieties. As expected, no helical packing was observed in the crystal structure.
197 Therefore, the structure of σNS-ΔN17 suggests that the N-terminal arm and the core of WT σNS
198 operate as independent structural units, and removing the N-terminal arm does not alter the
199 dimeric association of the core. Collectively, the three crystal structures provide strong evidence
200 that (i) WT σNS has a tendency to form dimers, (ii) the dimer is the basic unit of multimeric
201 assembly, and (iii) domain-swapping interactions of the flexible N-terminal arms are required to
202 link the dimeric units to form a multimer. Furthermore, the σNS-ΔN17 structure showed that bile

203 acid derivatives bind to the same location in σNS as the N-terminal arms in the σNS-R6A
204 structure (**Fig. 5g**), suggesting that this location in the σNS core domain has intrinsic affinity for
205 cholesterol-like molecules and that binding to such molecules disrupts filamentous helical
206 assemblies by competing with the binding of the N-terminal arms.
207
208 **σNS oligomer exhibits RNA chaperone activity**
209 The surface representation of the helical assembly in the Se-Met σNS-R6A structure shows a
210 negatively charged exterior (**Fig. 6a**) and a positively charged interior (**Fig. 6b**). A cutaway view
211 of the central tunnel of the helical assembly reveals a substantial number of positively charged
212 residues, suggesting that this region can bind RNA by electrostatic interactions. *In silico* docking
213 experiments demonstrated that the central tunnel can accommodate an RNA strand surrounded
214 by σNS dimers (**Fig. 6c-e**). This finding, coupled with previous studies showing that avian
215 reovirus σNS displays RNA-chaperone activity[16], prompted us to hypothesize that mammalian
216 orthoreovirus σNS is likewise an RNA chaperone. To test this hypothesis, we first examined
217 whether purified WT σNS and σNS-R6A disrupt dsRNA by incubating each of these σNS
218 proteins with an RNA-RNA duplex with an overhang of 6 nucleotides on either side. After
219 incubation, the reaction mixtures were treated with proteinase K and resolved by electrophoresis
220 in nondenaturing polyacrylamide gels. The RNA-RNA duplex migrated as a single prominent
221 band when σNS was not added to the reaction mixtures (**Fig. 6f**). However, following addition of
222 increasing concentrations of WT σNS, we observed a proportional increase in the formation of
223 ssRNA molecules. As an important control, formation of ssRNA was not observed in a similar
224 experiment using σNS-R6A (**Fig. 6g**). These results indicate that σNS catalyzes formation of
225 ssRNA molecules from dsRNA and that σNS displays RNA-destabilizing activity. We next

226 evaluated whether σNS is capable of annealing two ssRNA molecules to form dsRNA. In this
227 experiment, we observed a proportional increase in the formation of dsRNA molecules following
228 addition of increasing concentrations of WT σNS to the reaction mixtures (**Fig. 6h**), indicating
229 that σNS catalyzed formation of dsRNA molecules from ssRNA and thus possesses RNA-
230 annealing activity. Since the reaction buffer for these experiments contained no ATP, the RNA
231 chaperone activity of σNS is independent of energy input. These experiments demonstrate that
232 σNS is not a helicase but an RNA chaperone.
233
234 **Binding of bile acid inhibits σNS chaperone activity**
235 From our observation that bile acid binding disrupts formation of filamentous helical assemblies
236 of σNS, we hypothesized that bile acid binding would impede σNS RNA chaperone activity. To
237 test this hypothesis, we conducted RNA chaperone assays following incubation of σNS with
238 different components of bile acid derivatives, including taurocholic acid sodium salt hydrate
239 (TASAH), sodium glycocholate hydrate (SGAH), 3-[(3-cholamidopropyl)dimethylammonio]-1-
240 propanesulfonate (CHAPS), and 3-[(3-cholamidopropyl)dimethylammonio]-2-hydroxy-1-
241 propanesulfonate (CHAPSO). Each of these components reduced the RNA-destabilizing activity
242 of σNS to varying degrees (**Fig. 6h**), suggesting that the RNA chaperone activity of σNS requires
243 formation of filament-like assemblies. As anticipated, σNS RNA-binding capacity and oligomer
244 formation were abolished by removal of the N-terminal 17 residues and, concomitantly, the
245 σNS-ΔN17 mutant did not display RNA chaperone activity (**Fig. 6i**).
246
247 **Discussion**

248 VFs serve an essential function in the replication of many viruses, as these structures house viral
249 genome synthesis and assembly of progeny virions. In the case of mammalian orthoreoviruses,
250 two nonstructural proteins, σNS and μNS, initiate VF formation, and σNS recruits viral RNAs
251 into these compartments. Our crystallographic and biochemical studies reported here provide a
252 mechanistic understanding of how σNS forms filamentous assemblies by linking dimeric units
253 through domain-swapping interactions of the N-terminal arms and further how such a multimeric
254 association is required for the RNA-helix destabilizing and annealing activities of σNS. These
255 findings implicate σNS in unwinding viral RNA for loading into the viral RNA-dependent RNA
256 polymerase during genome replication and promoting interactions between the viral RNAs to
257 facilitate their selective encapsidation during virion assembly.
258
259 **Higher-order oligomers and a flexible element–a common theme in VF formation?**
260 Although distinct in its structure, σNS displays several functional and mechanistic similarities
261 with other dsRNA virus nonstructural proteins, such as rotavirus NSP2 and rice black-streaked
262 dwarf virus (RBSDV) P9-1. Like σNS, both NSP2 and P9-1 are implicated in formation of VFs.
263 The striking common structural feature of these proteins is the formation of oligomeric
264 assemblies requiring a flexible structural element. However, they differ in detail. Unlike the
265 formation of filamentous assemblies by σNS, rotavirus NSP2 forms a donut-shaped octamer [17,18].
266 Instead of the flexible N-terminal arm of σNS, which is responsible for dimer-dimer association
267 in filamentous assembly formation, NSP2 has a flexible C-terminal arm, which facilitates inter-
268 octamer association through domain-swapping interactions with neighboring NSP2 molecules [17].
269 Formation of higher-order NSP2 octamers is thought to be the basis for VF formation during
270 rotavirus replication [17,19]. RBSDV P9-1 also forms an octamer using a flexible C-terminal arm[20-

271 [22]. Like rotavirus NSP2, higher-order P9-1 octamers are required for formation of VFs, as
272 deletion of this sequence disrupts RBSDV VFs [22]. From our studies, deletion of the N-terminal
273 arm of σNS abrogates dimer-dimer interactions and precludes formation of higher-order
274 multimers. However, further experiments are required to assess the function of the flexible N-
275 terminal arm in the formation of functional VFs.
276
277 **RNA chaperone activity–a flexible N-terminal arm**
278 An important finding from our studies is that mammalian orthoreovirus σNS exhibits helix-
279 destabilizing and RNA-annealing activities without requiring a metal ion or ATP, which makes
280 this protein a *bona fide* RNA chaperone [24]. Similar RNA chaperone activity has been reported for
281 rotavirus NSP2 [25] and avian reovirus σNS [16]. The RNA duplex used in our experiments contains
282 overhangs at the ends of both strands, suggesting that passive strand displacement activity is
283 initiated after σNS binds to unduplexed overhang regions. The binding of σNS would then
284 prevent reannealing of the duplex and further separate the two strands. Using complementary
285 single-stranded RNAs, our studies show that σNS binds, unfolds, and releases these molecules to
286 facilitate formation of duplex RNA.
287 The RNA chaperone activity of σNS requires the flexible N-terminal arm with an
288 arginine at residue 6 to function in domain-swapping interactions, as the R6A substitution or
289 deletion of the N-terminal arm curtails this activity. In an analogous scenario, deletion of the
290 flexible C-terminal arm of NSP2 also significantly reduces RNA chaperone activity [26]. Thus, the
291 requirement for a flexible region in these proteins suggests that the mechanism is likely mediated
292 by disorder or entropy transfer. One possibility is that σNS uses the flexibility of the N-terminal
293 arm for binding RNA and subsequently releases the bound RNA. Such a possibility is consistent

294 with our observation that a single residue, Arg 6, in the N-terminal arm influences the RNA-
295 binding capacity of σNS [8]. The free N-terminal arms of the σNS multimer subunits (**Fig. 5e**)
296 likely exist in a dynamic equilibrium between a freely exposed open state, in which Arg 6 can
297 initiate binding to RNA, and a closed state, in which the N-terminal arm is engaged in domain-
298 swapping interactions for RNA release. Such dynamics also may allow the N-terminal arm to
299 recruit free σNS dimers to elongate the multimer and coat the RNA as a mechanism for
300 unwinding (**Fig. 7**). The dynamics and preference between open and closed states are likely
301 influenced by the presence of RNA and buffer conditions (pH and ionic strength). This idea is
302 consistent with our observation that in solution σNS exists as an octamer in the absence of RNA,
303 but in the presence of RNA, as observed in our previous cryo-EM images [12], σNS forms
304 filamentous structures of varying lengths.
305

306 **Bile acid binding–tampering with the flexibility of the N-terminal arm**

307 A serendipitous but fascinating finding from our study is that bile acid derivatives bind to the
308 same site in σNS as the N-terminal arm and impede the RNA chaperone activity of σNS (**Fig.**
309 **5h**). These findings are consistent with the proposed mechanism of σNS RNA chaperone
310 activity. First, the σNS crystal structure shows that the free N-terminal arm displaced by bile acid
311 is disordered, as the electron density for this region is absent in the presence of bile acid. This
312 observation is consistent with the disorder or entropy-transfer model of RNA chaperone activity
313 [27], in which entropy is transferred to bound RNA to facilitate RNA refolding. Second, our
314 finding that bile acid binding does not entirely abrogate RNA chaperone activity is consistent
315 with the idea that RNA modulates the kinetics of open and closed states of the N-terminal σNS
316 arm. It is possible that differences in the efficiency by which bile salts diminish RNA chaperone

317 activity are determined by differences in the capacity of these molecules to compete with the N-
318 terminal arm in the presence of RNA.
319
320 **Role of RNA chaperone activity in reovirus replication**
321 Our discovery that σNS displays RNA chaperone activity raises an important question about the
322 stage in viral replication at which this activity is required. While the function of σNS RNA-
323 binding activity in the recruitment of viral RNAs to VFs has been established [8], further studies
324 are needed to unequivocally determine the precise function of σNS RNA chaperone activity. As
325 proposed for RNA chaperones of single-stranded RNA viruses [27], σNS RNA chaperone activity
326 may be necessary for unfolding viral mRNA for translation, replication, packaging, or some
327 combination of these steps. In the case of dsRNA viruses like reoviruses and rotaviruses that
328 package multiple dsRNA segments, RNA chaperone activity is likely essential for proper
329 refolding of the kinetically trapped intermediate structures in capped viral mRNAs to allow these
330 RNAs to serve as templates for dsRNA synthesis by the viral polymerase and also for facilitating
331 interactions between specific viral RNAs for gene segment assortment and packaging.
332
333 ## Methods
334 **Expression and purification of σNS constructs**
335 Synthesized genes for WT σNS, σNS-R6A, and σNS-ΔN17 were subcloned into the bacterial
336 expression vector pET28 with an N-terminal His tag and a TEV protease cleavage site (Epoch
337 Life Science). *Escherichia coli* DE3 cells (Novagen) were transformed with the pET28 plasmid
338 and induced with 0.5 mM isopropyl β-D-1-thiogalactopyranoside (IPTG) (Millipore Sigma)
339 when the optical density at 600 nm reached 0.6. *E. coli* B834 cells were incubated in Dream

340 medium supplemented to contain Dream Nutrient Mix and 10 mg/mL Se-Met. Cells were
341 resuspended in 50 mM Tris-HCl (pH 8.0), 300 mM NaCl, and 10 mM imidazole and
342 supplemented to contain a protease inhibitor cocktail (Roche). Cells were lysed using a
343 microfluidizer (Microfluidics), followed by removal of cell debris by centrifugation at 39,000 x *g*
344 at 4°C for 30 minutes. His-tagged σNS was loaded onto a Ni-NTA agarose column (Qiagen) and
345 eluted using a gradient of 50 mM Tris-HCl (pH 8.0), 300 mM NaCl, and 250 mM imidazole. The
346 eluted His-tagged σNS was concentrated using a 10-kDa centrifugal filter unit (Millipore),
347 dialyzed into 50 mM Tris-HCl (pH 8.0), 300 mM NaCl, and 10 mM imidazole, and incubated
348 with TEV protease at 4°C overnight. The cleaved protein mixture was reloaded onto a Ni-NTA
349 agarose column to remove the His-TEV protease and uncleaved His-σNS. Cleaved σNS was
350 subjected to ion-exchange chromatography using a Q-column (GE Healthcare) and eluted with
351 20 mM Tris-HCl (pH 8.0) and 1 M NaCl. Eluted σNS was separated using an S200 16/60-
352 increase column in 10 mM HEPES (pH 8.0) and 150 mM NaCl.
353
354 **Crystallization, data processing, structure determination, and refinement**
355 Freshly purified Se-Met σNS-R6A, native σNS-R6A, and σNS-ΔN17 were used for initial
356 crystallization screens immediately following size-exclusion chromatography. In each case,
357 fractions with σNS proteins were collected and concentrated to ~ 10 mg/mL in buffer containing
358 10 mM HEPES (pH 8.0) and 150 mM NaCl for crystallization. Crystals were propagated at 20°C
359 by hanging-drop vapor diffusion using a Mosquito crystallization robot (TTP LabTech) and
360 imaged using a Rock Imager (Formulatrix). Each drop contained 0.2 µL of the σNS protein and
361 0.2 µL of crystallization buffer. Se-Met σNS-R6A produced crystals in the condition containing
362 0.1 M MES monohydrate (pH 6.5) and 1.6 M magnesium sulfate heptahydrate (Hampton

363 Research), whereas native σNS-R6A and σNS-ΔN17 crystallized in the condition with 1.2 %
364 cholic acid derivatives mix, 0.1 M Buffer System 3 (pH 8.5), and 30 % Precipitant Mix 3
365 (Morpheus III, Molecular Dimensions). Crystals were transferred into a cryoprotectant solution
366 with 20% glycerol and flash-frozen in liquid nitrogen. X-ray diffraction data for σNS were
367 collected on beamline 5.0.1 at the Advanced Light Source at the Lawrence Berkeley National
368 Laboratory. Diffraction data were processed using the CCP4 software suite [28]. For Se-Met σNS-
369 R6A, phases and initial electron density maps were calculated by single-wavelength anomalous
370 diffraction (SAD) phasing using SHELX [29], and automated model building with experimental
371 phases was conducted using ARP/wARP [30] before iterative cycles of manual model building and
372 refinement using COOT[31] and PHENIX [32]. Further model building was accomplished using
373 COOT based on the difference maps [31] (see validation report for PDB id: 8TKA). The structures
374 of native σNS-R6A and σNS-ΔN17 were determined using molecular replacement with PHENIX
375 [32]. The bile acid binding in these structures was validated by omit maps (see validation reports
376 for PDB id: 8TL8 and 8TL1). Data collection and refinement statistics following the final
377 refinement cycle are provided in Supplementary Table 1. Interactions between σNS and colic
378 acid derivatives were analyzed using LigPlot+ v.2.1 [33]. Figures were prepared using Chimera [34].

379

380 **RNA helix destabilizing assay**

381 RNA helix destabilizing assays were conducted as described [35] with modifications. Various
382 concentrations of σNS, σNS-R6A, and σNS-ΔN17 (2.5 to 20 μM) and 0.5 μM dsRNA substrate
383 were incubated at 37°C for 1 h with 25 mM HEPES-KOH (pH 8.0), 100 mM NaCl, 2 mM
384 $MgCl_2$, 2 mM DTT, and 5 U RNase-OUT in a reaction volume of 20 μL. Reactions were
385 terminated by the addition of 5 U proteinase K for 15 min and 2.5 μL 5 × loading buffer (100

386 mM Tris–HCl [pH 7.5], 50% glycerol, and bromophenol blue) and electrophoresed in 4-20%
387 native polyacrylamide gels. Gels were scanned using a Typhoon 9200 imager (GE Healthcare).
388 The effect of bile acids on σNS RNA helix destabilizing activity was determined by incubating
389 20 and 40 μM of different components of bile acid derivatives, including TASAH, SGAH,
390 CHAPS, and CHAPSO, with 20 μM σNS for 1 h prior to initiation of the helix destabilization
391 assay.

392

393 **RNA strand hybridization assay**

394 Various concentrations of σNS (2.5 to 20 μM) were incubated with HEX-labeled and unlabeled
395 RNA strands (0.5 μM each strand) at 37°C for 1 h in 50 mM HEPES-KOH (pH 8.0), 2.5 mM
396 $MgCl_2$, 2 mM DTT, 0.01% BSA, and 5 U RNase-OUT in a reaction volume of 20 μl. Reactions
397 were terminated as described for RNA helix destabilizing assays. Two complementary stem-
398 loop-structured RNA strands were used for hybridization assays [35]. Reactions were resolved in 4-
399 20% native polyacrylamide gels and scanned using a Typhoon 9200 imager.

400

401 ## Acknowledgements

402 We are grateful to members of the Dermody and Prasad laboratories for many useful discussions.
403 This work was supported by U.S. Public Health Service award R01 AI032539, the Heinz
404 Endowments (T.S.D.), and grant Q1279 from Robert Welch Foundation (B.V.V.P). We
405 acknowledge the Advanced Light Source (8.2.2) (Berkeley, CA) for X-ray data collection. The
406 ALS-ENABLE beamlines are supported in part by U.S. Public Health Service award P30
407 GM124169. The Advanced Light Source is a Department of Energy Office of Science User

Facility under Contract No. DE-AC02-05CH11231. The funders had no role in study design, data collection and analysis, decision to publish, or preparation of the manuscript.

Author contributions

B.Z. and L.H. conceived, designed, and conducted experiments, analyzed data, contributed materials and analytic tools, and drafted the paper. S.K., N.N., C.H.L., X.S., and G.M.T. conceived and designed experiments, analyzed data, and contributed materials and analytic tools. T.S.D. and B.V.V.P. conceived and designed experiments, analyzed the data, and drafted the paper. All authors reviewed, critiqued, and provided comments on the manuscript.

Competing interests

The authors declare no competing interests.

Additional information

Supplementary information Supplementary Table 1.

Correspondence and requests for materials should be addressed to Terence S. Dermody or B. V. Venkataram Prasad.

426 ## Figure Legends

427

428 **Fig. 1 Purification of σNS-R6A dimer.** Elution profiles of WT σNS and σNS-R6A after **a**
429 anion-exchange chromatography and **b** size-exclusion chromatography. A size shift is observed
430 with the different elution volumes for each peak.

431

432 **Fig. 2 Crystal structure of σNS contains a flexible N-terminal arm. a** Ribbon and surface
433 representations of the σNS crystal structure. The N-terminal arm is demarcated in a grey-dotted
434 frame. **b** Topologic representation of the σNS crystal structure generated by the PDBsum
435 database. Strands are colored in green with a light blue background, helices are colored in cyan,
436 and the connecting loops are colored in grey. **c** The RMSF graph of the σNS dimer and the σNS
437 dimer in complex with an RNA molecule after 100 nanoseconds of molecular dynamics
438 simulations.

439

440 **Fig. 3 σNS dimer is the basic functional unit. a** Ribbon (left) and surface representations
441 (right) of the σNS dimer with subunits colored in green and blue. The N-terminal arms are
442 demarcated in grey-dotted frames. **b** Ribbon representation of the σNS dimer highlighting
443 residues that mediate interactions at the dimer interface inside a black frame in blue and green. **c**
444 Amino acid residues from the subunits at the dimer interface are colored blue and green.
445 Hydrogen bond interactions are shown by red lines.

446

447 **Fig. 4 Formation of σNS filaments. a** Surface representation of the helical assembly formed by
448 σNS dimers using crystallographic $P6_5$ symmetry. Dimers are depicted as blue and green

449 subunits. A single helical turn (80 Å in length) is demarcated in the purple-dotted frame. **b** A 90º
450 rotation around the horizontal axis perpendicular to the filament shows the central tunnel. The
451 tunnel is 40 Å in width, and the total diameter of the filament is 150 Å. **c** Single helical turn
452 formed by six σNS dimers. Dimers are depicted in different colors. One pair of interacting
453 dimers (pink and cyan) are demarcated in a yellow frame. The location of the N-terminal arm of
454 the pink dimer is shown within the red frame, with a red arrow pointing to the (**e**) Ligplot of
455 interactions between N-terminal arm residues of the pink dimer and core domain residues of the
456 blue dimer. Residues involved in hydrophobic interactions are shown by brick-red spoked arcs,
457 and hydrogen bond interactions between the residues are indicated by green lines, with carbon,
458 oxygen, and nitrogen atoms depicted in black, red, and blue, respectively. Note the involvement
459 of the Se-Met residue at position 1 (Mse 1), indicated by an asterisk. **d** Interacting dimers (pink
460 and blue) corresponding to the yellow frame in **c** are shown separately to illustrate how the N-
461 terminal arms (in red frame) project away in opposite directions (thick red arrows) to chain-link
462 the neighboring dimers to form the helical assembly shown in **Fig. 1a.**

463

464 **Fig. 5 Binding of bile acid derivatives disrupts σNS oligomerization and RNA-destabilizing**
465 **activity. a** Electrostatic representation of σNS-R6A in complex with bile acid derivatives (S1
466 and S2), colored in green. The grey-dotted box demarcates the missing disordered N-terminal
467 arm. **b, c** Residues mediating bile-acid-derivative binding at S1 and S2 defined by LigPlot
468 following the same notations as in **Fig. 4e** for hydrophobic and hydrogen bond interactions. Bile
469 acid derivatives are shown in purple bonds with carbon and oxygen atoms in black and red,
470 respectively. **c** The higher-order structure formed by crystal packing of σNS-R6A when bile acid
471 derivatives are present. **d** The helical assembly as observed in the crystal structure of Se-Met

472 σNS-R6A with dimeric subunits shown in pink and blue. **e** Close-up view of the N-terminal arm
473 (pink) interacting with a groove in the neighboring subunit (blue). **f** In the structure of σNS-R6A
474 in complex with bile acid derivatives, the same groove is occupied by a bile acid replacing the N-
475 terminal arm, which becomes disordered. **g** Electrostatic representations σNS-ΔN17 in complex
476 with two bile acid derivatives (in green) bound at the same location as in the σNS-R6A structure
477 shown in **Fig. 5a**. The grey-dotted box demarcates the missing N-terminal arm.

478

479 **Fig. 6 RNA chaperone activity of σNS. a** Electrostatic representation of a σNS filament with
480 red indicating negatively charged residues and blue indicating positively charged residues. The
481 exterior of the filament is negatively charged. **b** Cutaway view of the filament. The interior of the
482 filament is positively charged. **c** A single dimer is demarcated in a black-dotted frame with its
483 relative position within the filament. **d** A 90-degree rotation around the z-axis from the previous
484 position shows a side-view of the dimer. A docked RNA molecule is colored in yellow. **e** A 90-
485 degree rotation around the z-axis from the previous position shows the positively charged pocket
486 of σNS that binds to a docked RNA molecule colored in yellow. The black-dotted frame depicts
487 the position of the dimer within the filament. **f** RNA-helix destabilizing activity of WT σNS.
488 Boiling of the duplex disrupts duplex formation. Increasing concentrations of WT σNS yield
489 more ssRNA products. Maltose-binding protein (MBP) and norovirus (NV) P41 serve as
490 negative and positive controls, respectively. **g** RNA-helix destabilizing activity of σNS-R6A.
491 Increasing concentrations of σNS-R6A yield only limited ssRNA products. **h** RNA-annealing
492 activity of WT σNS. Boiling two ssRNA molecules promotes strand annealing. Similar levels of
493 annealing activity are observed following incubation with the highest concentration of WT σNS.
494 **i** Effects of each component of the bile acid derivatives on the RNA-destabilizing activity of

σNS. TASAH, taurocholic acid sodium salt hydrate. SGAH, sodium glycocholate hydrate. CHAPS, 3-[(3-cholamidopropyl)dimethylammonio]-1-propanesulfonate. CHAPSO, 3-[(3-cholamidopropyl)dimethylammonio]-2-hydroxy-1-propanesulfonate. **j** RNA-helix destabilizing activity of σNSΔ17. Increasing concentrations of σNS Δ17 does not yield significant ssRNA products.

Fig. 7 Model of σNS oligomerization, RNA binding, and RNA unfolding. The free N-terminal arms of σNS oligomers exist in equilibrium between an open state that can initiate RNA binding and a closed state that engages in domain-swapping interactions and RNA release from the N-terminal arm. The dynamics of the N-terminal arms allow for recruitment of free σNS dimers to elongating σNS oligomers to coat the RNA and enhance RNA unfolding.

References

1 Day, J. M. The diversity of the orthoreoviruses: molecular taxonomy and phylogentic divides. *Infection, genetics and evolution : journal of molecular epidemiology and evolutionary genetics in infectious diseases* **9**, 390-400 (2009). https://doi.org:10.1016/j.meegid.2009.01.011

2 Ouattara, L. A. *et al.* Novel human reovirus isolated from children with acute necrotizing encephalopathy. *Emerging infectious diseases* **17**, 1436-1444 (2011). https://doi.org:10.3201/eid1708.101528

3 Bouziat, R. *et al.* Reovirus infection triggers inflammatory responses to dietary antigens and development of celiac disease. *Science* **356**, 44-50 (2017). https://doi.org:10.1126/science.aah5298

4 DeAntoneo, C., Danthi, P. & Balachandran, S. Reovirus Activated Cell Death Pathways. *Cells* **11** (2022). https://doi.org:10.3390/cells11111757

5 Muller, L., Berkeley, R., Barr, T., Ilett, E. & Errington-Mais, F. Past, Present and Future of Oncolytic Reovirus. *Cancers (Basel)* **12** (2020). https://doi.org:10.3390/cancers12113219

524 6 Maginnis, M. S. *et al.* Beta1 integrin mediates internalization of mammalian reovirus. *J*
525 *Virol* **80**, 2760-2770 (2006). https://doi.org:10.1128/JVI.80.6.2760-2770.2006

526 7 Danthi, P. *et al.* From touchdown to transcription: the reovirus cell entry pathway.
527 *Current topics in microbiology and immunology* **343**, 91-119 (2010).
528 https://doi.org:10.1007/82_2010_32

529 8 Lee, C. H. *et al.* Reovirus Nonstructural Protein sigmaNS Recruits Viral RNA to
530 Replication Organelles. *mBio* **12**, e0140821 (2021). https://doi.org:10.1128/mBio.01408-
531 21

532 9 Desmet, E. A., Anguish, L. J. & Parker, J. S. Virus-mediated compartmentalization of the
533 host translational machinery. *mBio* **5**, e01463-01414 (2014).
534 https://doi.org:10.1128/mBio.01463-14

535 10 Choudhury, P., Bussiere, L. D. & Miller, C. L. Mammalian Orthoreovirus Factories
536 Modulate Stress Granule Protein Localization by Interaction with G3BP1. *J Virol* **91**
537 (2017). https://doi.org:10.1128/JVI.01298-17

538 11 Stamatos, N. M. & Gomatos, P. J. Binding to selected regions of reovirus mRNAs by a
539 nonstructural reovirus protein. *Proceedings of the National Academy of Sciences of the*
540 *United States of America* **79**, 3457-3461 (1982).

541 12 Zamora, P. F. *et al.* Reovirus Nonstructural Protein sigmaNS Acts as an RNA Stability
542 Factor Promoting Viral Genome Replication. *J Virol* **92** (2018).
543 https://doi.org:10.1128/JVI.00563-18

544 13 Goral, M. I., Mochow-Grundy, M. & Dermody, T. S. Sequence diversity within the
545 reovirus S3 gene: reoviruses evolve independently of host species, geographic locale, and
546 date of isolation. *Virology* **216**, 265-271 (1996). https://doi.org:10.1006/viro.1996.0059

547 14 Larsen, T. A., Olson, A. J. & Goodsell, D. S. Morphology of protein-protein interfaces.
548 *Structure* **6**, 421-427 (1998). https://doi.org:10.1016/s0969-2126(98)00044-6

549 15 Martinez, J. *et al.* Selenomethionine incorporation into amyloid sequences regulates
550 fibrillogenesis and toxicity. *PLoS One* **6**, e27999 (2011).
551 https://doi.org:10.1371/journal.pone.0027999

552 16 Borodavka, A., Ault, J., Stockley, P. G. & Tuma, R. Evidence that avian reovirus
553 sigmaNS is an RNA chaperone: implications for genome segment assortment. *Nucleic*
554 *Acids Res* **43**, 7044-7057 (2015). https://doi.org:10.1093/nar/gkv639

555 17 Hu, L. *et al.* Crystallographic analysis of rotavirus NSP2-RNA complex reveals specific
556 recognition of 5' GG sequence for RTPase activity. *J Virol* **86**, 10547-10557 (2012).
557 https://doi.org:10.1128/JVI.01201-12

558 18 Jayaram, H., Taraporewala, Z., Patton, J. T. & Prasad, B. V. Rotavirus protein involved
559 in genome replication and packaging exhibits a HIT-like fold. *Nature* **417**, 311-315
560 (2002). https://doi.org:10.1038/417311a

561 19 Criglar, J. M. *et al.* Phosphorylation cascade regulates the formation and maturation of
562 rotaviral replication factories. *Proceedings of the National Academy of Sciences of the*
563 *United States of America* **115**, E12015-E12023 (2018).
564 https://doi.org:10.1073/pnas.1717944115

565 20 Akita, F. *et al.* Crystallographic analysis reveals octamerization of viroplasm matrix
566 protein P9-1 of Rice black streaked dwarf virus. *J Virol* **86**, 746-756 (2012).
567 https://doi.org:10.1128/JVI.00826-11

568 21 Li, X. *et al.* Characterization of the importance of terminal residues for southern rice
569 black-streaked dwarf virus P9-1 viroplasm formations. *Protein Expr Purif* **111**, 98-104
570 (2015). https://doi.org:10.1016/j.pep.2015.04.003

571 22 Wu, J. *et al.* Viroplasm protein P9-1 of Rice black-streaked dwarf virus preferentially
572 binds to single-stranded RNA in its octamer form, and the central interior structure
573 formed by this octamer constitutes the major RNA binding site. *J Virol* **87**, 12885-12899
574 (2013). https://doi.org:10.1128/JVI.02264-13

575 23 Parker, J. S., Broering, T. J., Kim, J., Higgins, D. E. & Nibert, M. L. Reovirus core
576 protein mu2 determines the filamentous morphology of viral inclusion bodies by
577 interacting with and stabilizing microtubules. *J Virol* **76**, 4483-4496 (2002).
578 https://doi.org:10.1128/jvi.76.9.4483-4496.2002

579 24 Semrad, K. Proteins with RNA chaperone activity: a world of diverse proteins with a
580 common task-impediment of RNA misfolding. *Biochem Res Int* **2011**, 532908 (2011).
581 https://doi.org:10.1155/2011/532908

582 25 Bravo, J. P. K. *et al.* Structural basis of rotavirus RNA chaperone displacement and RNA
583 annealing. *Proceedings of the National Academy of Sciences of the United States of*
584 *America* **118** (2021). https://doi.org:10.1073/pnas.2100198118

585 26 Coria, A. *et al.* Rotavirus RNA chaperone mediates global transcriptome-wide increase in
586 RNA backbone flexibility. *Nucleic Acids Res* **50**, 10078-10092 (2022).
587 https://doi.org:10.1093/nar/gkac738

588 27 Zuniga, S., Sola, I., Cruz, J. L. & Enjuanes, L. Role of RNA chaperones in virus
589 replication. *Virus Res* **139**, 253-266 (2009).
590 https://doi.org:10.1016/j.virusres.2008.06.015

591 28 Agirre, J. *et al.* The CCP4 suite: integrative software for macromolecular crystallography.
592 *Acta Crystallogr D Struct Biol* **79**, 449-461 (2023).
593 https://doi.org:10.1107/S2059798323003595

29 Uson, I. & Sheldrick, G. M. An introduction to experimental phasing of macromolecules illustrated by SHELX; new autotracing features. *Acta Crystallogr D Struct Biol* **74**, 106-116 (2018). https://doi.org:10.1107/S2059798317015121

30 Langer, G., Cohen, S. X., Lamzin, V. S. & Perrakis, A. Automated macromolecular model building for X-ray crystallography using ARP/wARP version 7. *Nat Protoc* **3**, 1171-1179 (2008). https://doi.org:10.1038/nprot.2008.91

31 Emsley, P., Lohkamp, B., Scott, W. G. & Cowtan, K. Features and development of Coot. *Acta Crystallogr D Biol Crystallogr* **66**, 486-501 (2010). https://doi.org:10.1107/S0907444910007493

32 Adams, P. D. *et al.* PHENIX: a comprehensive Python-based system for macromolecular structure solution. *Acta Crystallogr D Biol Crystallogr* **66**, 213-221 (2010). https://doi.org:10.1107/S0907444909052925

33 Laskowski, R. A. & Swindells, M. B. LigPlot+: multiple ligand-protein interaction diagrams for drug discovery. *J Chem Inf Model* **51**, 2778-2786 (2011). https://doi.org:10.1021/ci200227u

34 Pettersen, E. F. *et al.* UCSF Chimera--a visualization system for exploratory research and analysis. *J Comput Chem* **25**, 1605-1612 (2004). https://doi.org:10.1002/jcc.20084

35 Yang, J. *et al.* A cypovirus VP5 displays the RNA chaperone-like activity that destabilizes RNA helices and accelerates strand annealing. *Nucleic Acids Res* **42**, 2538-2554 (2014). https://doi.org:10.1093/nar/gkt1256

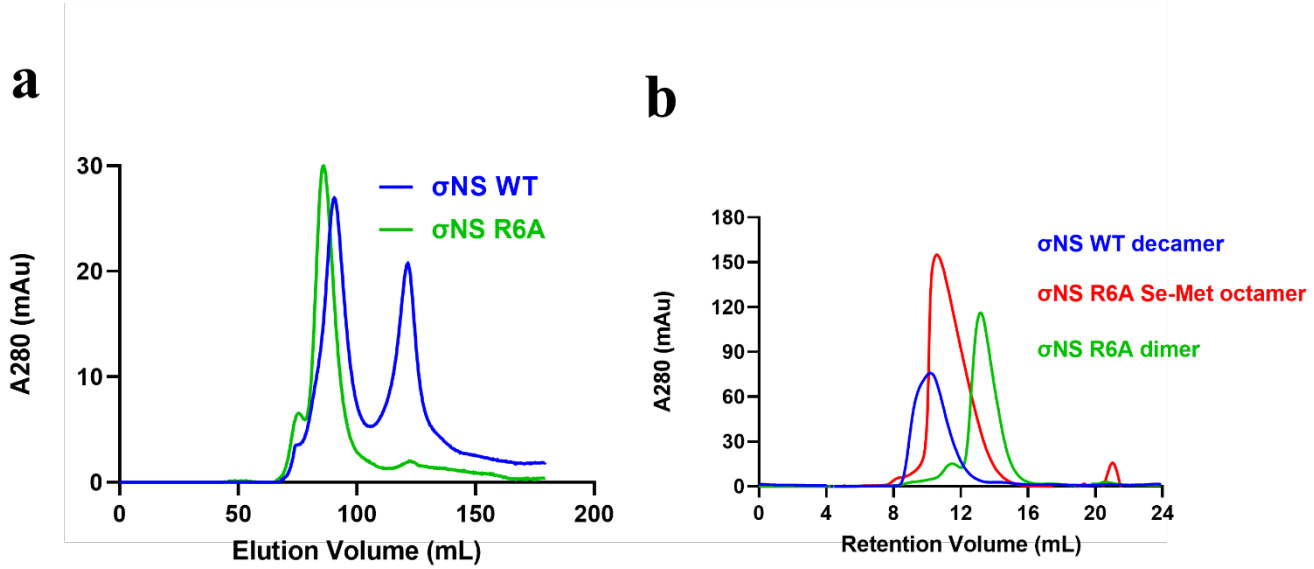

Fig. 1 Purification of σNS-R6A dimer. Elution profiles of WT σNS and σNS-R6A after **a** anion-exchange chromatography and **b** size-exclusion chromatography. A size shift is observed with the different elution volumes for each peak.

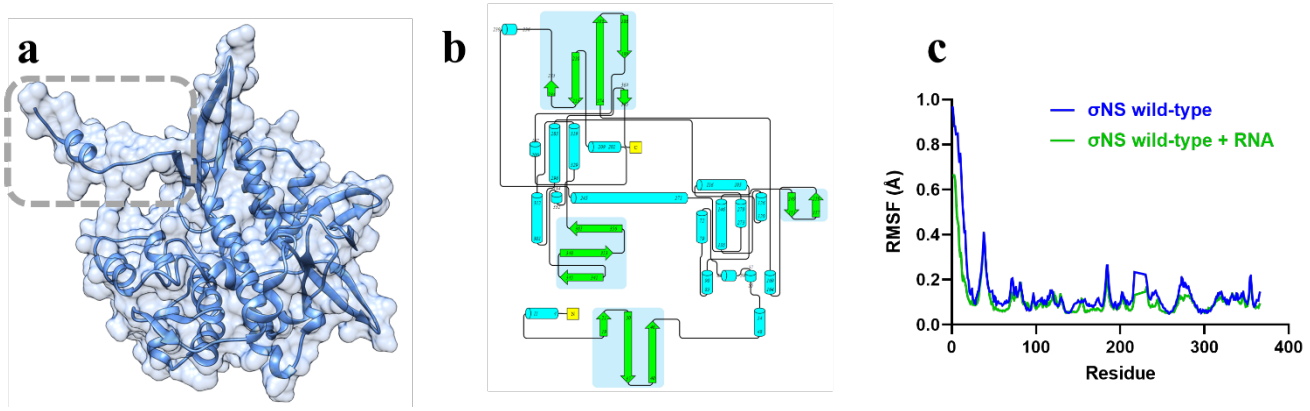

Fig. 2 Crystal structure of σNS contains a flexible N-terminal arm. a Ribbon and surface representations of the σNS crystal structure. The N-terminal arm is demarcated in a grey-dotted frame. **b** Topologic representation of the σNS crystal structure generated by the PDBsum database. Strands are colored in green with a light blue background, helices are colored in cyan, and the connecting loops are colored in grey. **c** The RMSF graph of the σNS dimer and the σNS dimer in complex with an RNA molecule after 100 nanoseconds of molecular dynamics simulations.

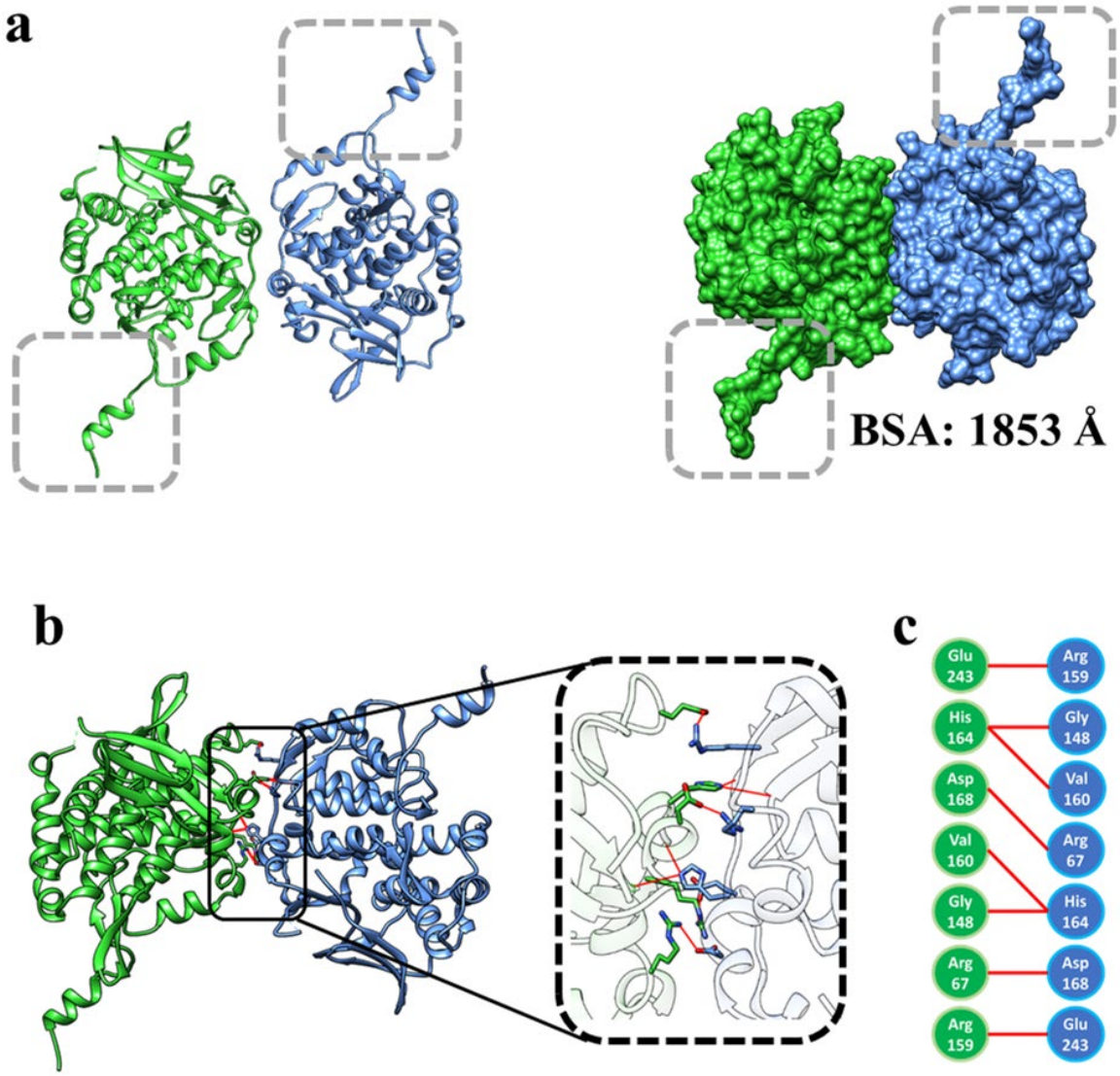

Fig. 3 σNS dimer is the basic functional unit. a Ribbon (left) and surface representations (right) of the σNS dimer with subunits colored in green and blue. The N-terminal arms are demarcated in grey-dotted frames. **b** Ribbon representation of the σNS dimer highlighting residues that mediate interactions at the dimer interface inside a black frame in blue and green. **c** Amino acid residues from the subunits at the dimer interface are colored blue and green. Hydrogen bond interactions are shown by red lines.

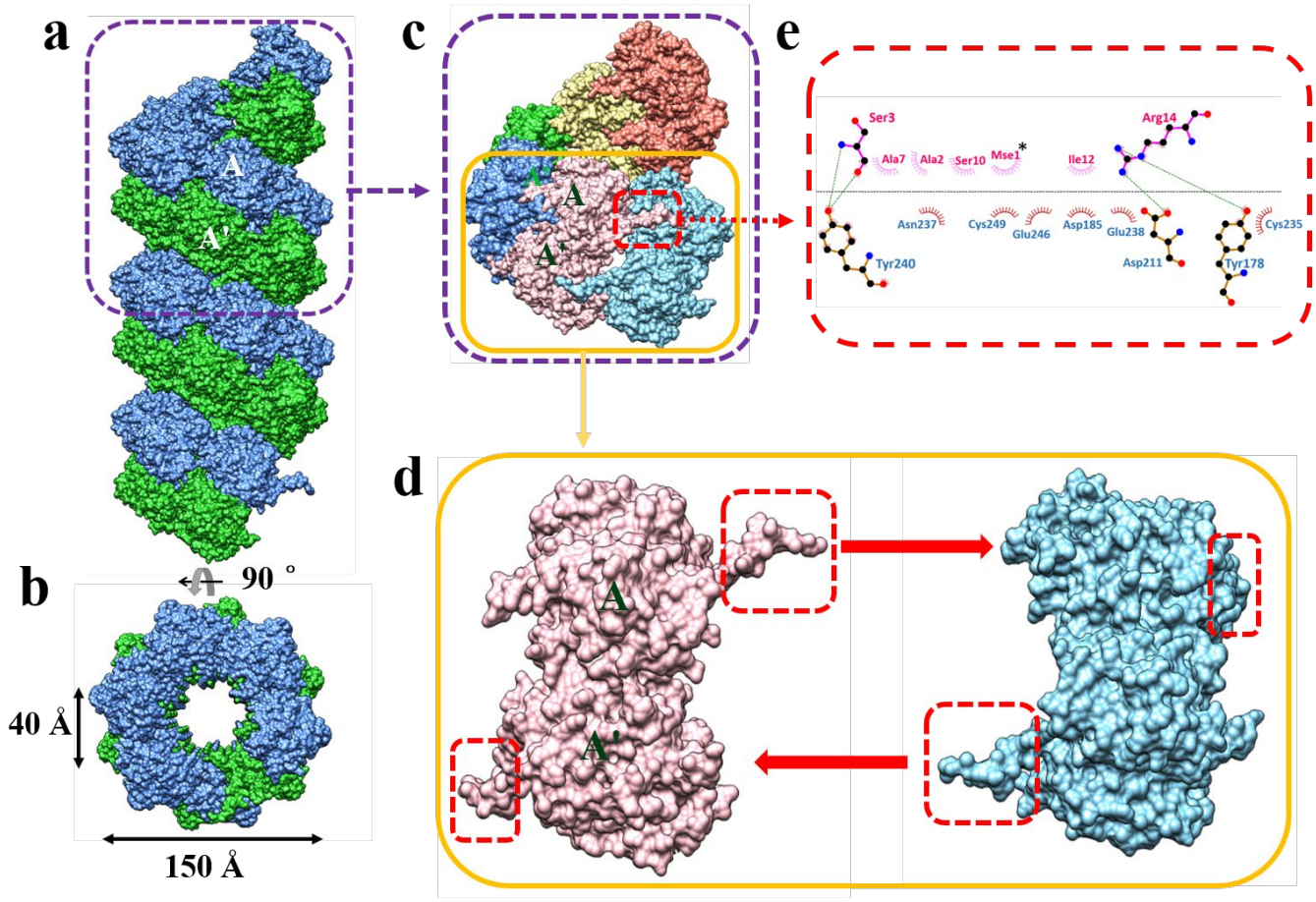

Fig. 4 Formation of σNS filaments. a Surface representation of the helical assembly formed by σNS dimers using crystallographic $P6_5$ symmetry. Dimers are depicted as blue and green subunits. A single helical turn (80 Å in length) is demarcated in the purple-dotted frame. **b** A 90º rotation around the horizontal axis perpendicular to the filament shows the central tunnel. The tunnel is 40 Å in width, and the total diameter of the filament is 150 Å. **c** Single helical turn formed by six σNS dimers. Dimers are depicted in different colors. One pair of interacting dimers (pink and cyan) are demarcated in a yellow frame. The location of the N-terminal arm of the pink dimer is shown within the red frame, with a red arrow pointing to the (**e**) Ligplot of interactions between N-terminal arm residues of the pink dimer and core domain residues of the blue dimer. Residues involved in hydrophobic interactions are shown by brick-red spoked arcs, and hydrogen bond interactions between the residues are indicated by green lines, with carbon, oxygen, and nitrogen atoms depicted in black, red, and blue, respectively. Note the involvement of the Se-Met residue at position 1 (Mse 1), indicated by an asterisk. **d** Interacting dimers (pink and blue) corresponding to the yellow frame in **c** are shown separately to illustrate how the N-terminal arms (in red frame) project away in opposite directions (thick red arrows) to chain-link the neighboring dimers to form the helical assembly shown in **Fig. 1a.**

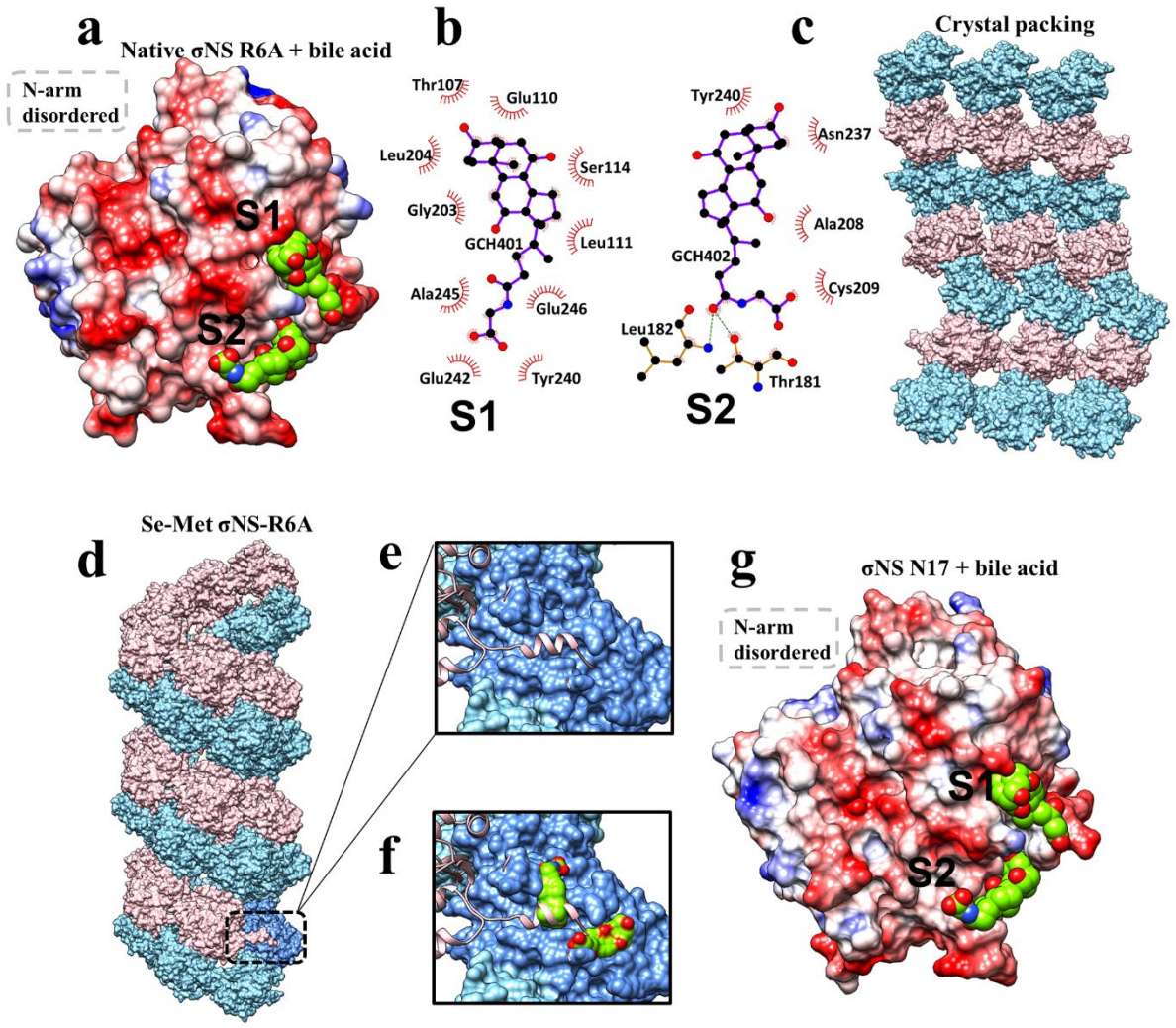

Fig. 5 Binding of bile acid derivatives disrupts σNS oligomerization and RNA-destabilizing activity. a Electrostatic representation of σNS-R6A in complex with bile acid derivatives (S1 and S2), colored in green. The grey-dotted box demarcates the missing disordered N-terminal arm. **b, c** Residues mediating bile-acid-derivative binding at S1 and S2 defined by LigPlot following the same notations as in **Fig. 4e** for hydrophobic and hydrogen bond interactions. Bile acid derivatives are shown in purple bonds with carbon and oxygen atoms in black and red, respectively. **c** The higher-order structure formed by crystal packing of σNS-R6A when bile acid derivatives are present. **d** The helical assembly as observed in the crystal structure of Se-Met σNS-R6A with dimeric subunits shown in pink and blue. **e** Close-up view of the N-terminal arm (pink) interacting with a groove in the neighboring subunit (blue). **f** In the structure of σNS-R6A in complex with bile acid derivatives, the same groove is occupied by a bile acid replacing the N-terminal arm, which becomes disordered. **g** Electrostatic representations σNS-ΔN17 in complex with two bile acid derivatives (in green) bound at the same location as in the σNS-R6A structure shown in **Fig. 5a**. The grey-dotted box demarcates the missing N-terminal arm.

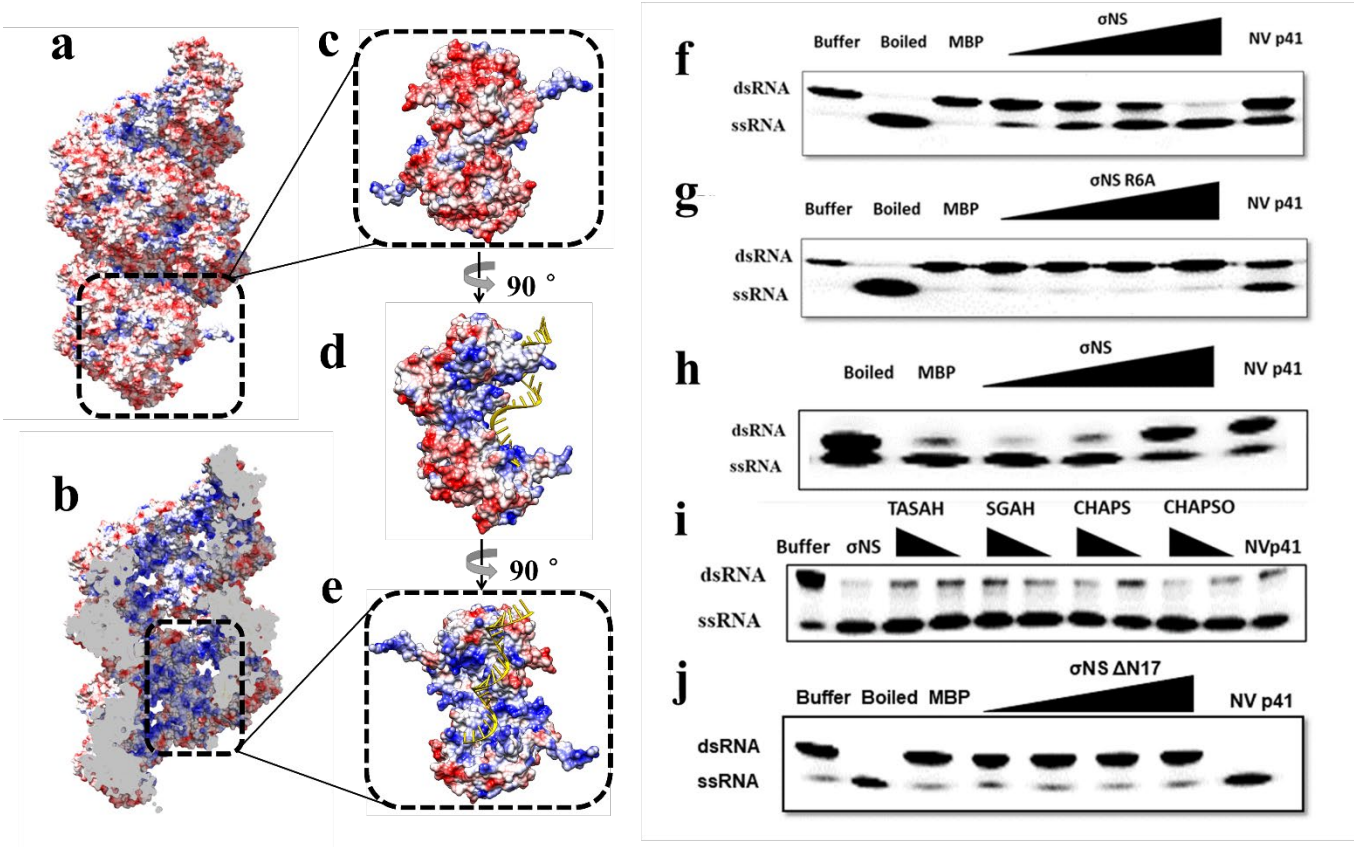

Fig. 6 RNA chaperone activity of σNS. a Electrostatic representation of a σNS filament with red indicating negatively charged residues and blue indicating positively charged residues. The exterior of the filament is negatively charged. **b** Cutaway view of the filament. The interior of the filament is positively charged. **c** A single dimer is demarcated in a black-dotted frame with its relative position within the filament. **d** A 90-degree rotation around the z-axis from the previous position shows a side-view of the dimer. A docked RNA molecule is colored in yellow. **e** A 90-degree rotation around the z-axis from the previous position shows the positively charged pocket of σNS that binds to a docked RNA molecule colored in yellow. The black-dotted frame depicts the position of the dimer within the filament. **f** RNA-helix destabilizing activity of WT σNS. Boiling of the duplex disrupts duplex formation. Increasing concentrations of WT σNS yield more ssRNA products. Maltose-binding protein (MBP) and norovirus (NV) P41 serve as negative and positive controls, respectively. **g** RNA-helix destabilizing activity of σNS-R6A. Increasing concentrations of σNS-R6A yield only limited ssRNA products. **h** RNA-annealing activity of WT σNS. Boiling two ssRNA molecules promotes strand annealing. Similar levels of annealing activity are observed following incubation with the highest concentration of WT σNS. **i** Effects of each component of the bile acid derivatives on the RNA-destabilizing activity of σNS. TASAH, taurocholic acid sodium salt hydrate. SGAH, sodium glycocholate hydrate. CHAPS, 3-[(3-cholamidopropyl)dimethylammonio]-1-propanesulfonate. CHAPSO, 3-[(3-cholamidopropyl)dimethylammonio]-2-hydroxy-1-propanesulfonate. **j** RNA-helix destabilizing activity of σNSΔ17. Increasing concentrations of σNS Δ17 does not yield significant ssRNA products.

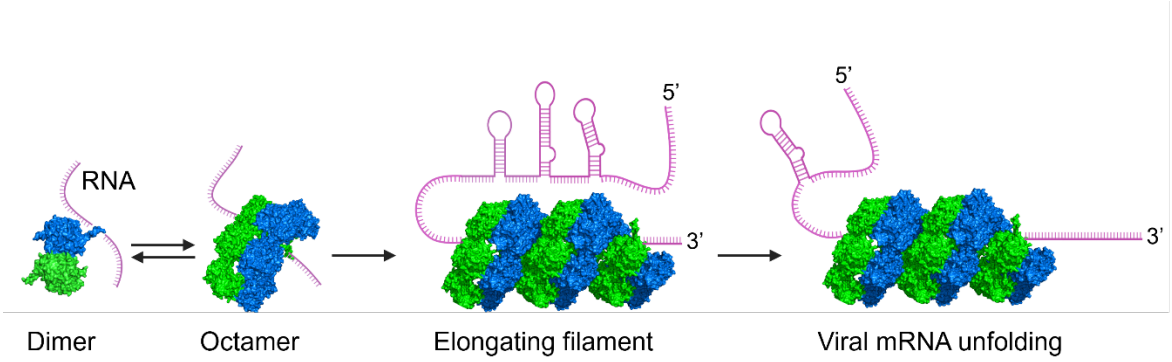

Fig. 7 Model of σNS oligomerization, RNA binding, and RNA unfolding. The free N-terminal arms of σNS oligomers exist in equilibrium between an open state that can initiate RNA binding and a closed state that engages in domain-swapping interactions and RNA release from the N-terminal arm. The dynamics of the N-terminal arms allow for recruitment of free σNS dimers to elongating σNS oligomers to coat the RNA and enhance RNA unfolding.

Table 1: X-ray diffraction data and structure refinement statistics

PDB ID	8TKA	8TL8	8TL1
Wavelength (Å)	0.99	0.99	0.99
Resolution range (Å)	34.28 – 3.0 (3.10 - 3.0)	34.22 - 3.20 (3.31 -3.20)	34.52-3.16 (3.27 - 3.16)
Space group	P 6_5	P 4_1	C 1 2 1
Unit cell			
a, b, c (Å)	137.11, 137.11, 98.24	54.12, 54.12, 305.52	77.52, 76.80, 89.09
α, ββ, γγ (°)	90, 90, 120	90, 90, 90	90, 94.27, 90
Unique reflections	41331 (4152)	11801 (1150)	7841 (302)
Multiplicity	2.0 (2.0)	1.0 (1.0)	1.0 (1.0)
Completeness (%)	99.77 (99.67)	81.91 (82.38)	86.39 (33.82)
Mean I/σ(I)	21.07 (3.53)	18.04 (5.40)	10.09 (3.21)
Wilson B-factor ($Å^2$)	68.54	62.51	67.74
R-merge (%)	0.0693	0.0311	0.1319
R-work (%)	0.2446 (0.3333)	0.2240 (0.2944)	0.208 (0.2561)
R-free (%)	0.2937 (0.4157)	0.2434 (0.2995)	0.250 (0.2895)
Number of non-hydrogen atoms	5494	5337	2708
Macromolecules	5494	5205	2637
Ligands	0	132	66
Solvent	0	0	5
Protein residues	708	669	336
R.M.S. deviations			
Bond lengths (Å)	0.012	0.005	0.010
Bond angles (°)	1.60	1.06	1.36
Ramachandran			
Favored (%)	96.29	2.57	95.48
Allowed (%)	3.14	2.57	3.61
Disallowed (%)	0.57	0.00	0.90
Average B-factor ($Å^2$)	81.30	59.23	67.73
Macromolecules	81.30	58.98	67.10
Ligand		69.46	95.72
Solvent			30.00

Numbers in parentheses correspond to the highest resolution range.